ELSEVIER

Journal of Photochemistry and Photobiology A: Chemistry 106 (1997) 105–111

Journal of PHOTOCHEMISTRY AND PHOTOBIOLOGY A: CHEMISTRY

Photochemistry relating to atmospheric reactions in the stratosphere

Masahiro Kawasaki *

Institute for Electronic Science and Graduate School of Environmental Science, Hokkaido University, Sapporo 060, Japan

Abstract

With a vacuum-UV-laser-induced fluorescence technique for $H(^2S)$, $D(^2S)$, $O(^3P_j)$, $O(^1D)$, $Cl(^2P_j)$ and $ClO(^2\Pi)$, the reactive species which induce atmospheric reactions in the stratosphere were measured directly in order to determine the dynamics of the photodissociation, reaction and quenching processes with HCl, O_2, O_3, CO, N_2, RH, RCl, chlorofluoromethanes, hydrochlorofluoromethanes and rare gases. It is suggested that the contribution of translationally hot atoms as well as vibrationally hot radicals and molecules will be important even under atmospheric conditions. Hot ozone can absorb UV photons longer than 310 nm, generating $O(^1D)$ atoms with an appreciable quantum yield. The translational relaxation rate of hot $O(^1D)$ is comparable with the quenching rate of $O(^1D)$ to $O(^3P)$. Not only ambient but also hot $O(^1D)$ atoms react with atmospherically important species. Highly vibrationally excited ClO radicals are also produced in the reaction of $Cl + O_3$. © 1997 Elsevier Science S.A.

Keywords: Atmospheric reactions; Photochemistry; Stratosphere

1. Introduction

The atmosphere is a giant photochemical reactor in which the light source is the sun. Stratospheric ozone at 20–50 km altitude is formed photochemically from O_2, and the layer structure owes its existence to peaks in both the absorption and reaction rates. The ''Chapman'' reactions, which include oxygen only, cannot explain the atmospheric ozone abundance due to catalytic loss processes by the atmospheric trace species ClO_x, HO_x and NO_x. The catalytic cycle involving ClO_x makes a major contribution to the destruction of odd oxygen in the mid-stratosphere, with the NO_x and HO_x cycles dominating in the lower and higher stratosphere respectively [1].

As shown in Fig. 1, these chemical cycles start with the photochemical reactions of oxygen, ozone, chlorine and chlorofluorocarbons

$$O_2 \xrightarrow{\hbar\omega} O(^1D) + O(^3P),$$
$$\xrightarrow{} 2O(^3P),$$

$$O_3 \xrightarrow{\hbar\omega} O(^1D) + O_2(a^1\Delta),$$
$$\xrightarrow{} O(^3P) + O_2(X^3\Sigma_g^-),$$

$$Cl_2,\ CFCs \xrightarrow{\hbar\omega} Cl + \cdots,$$

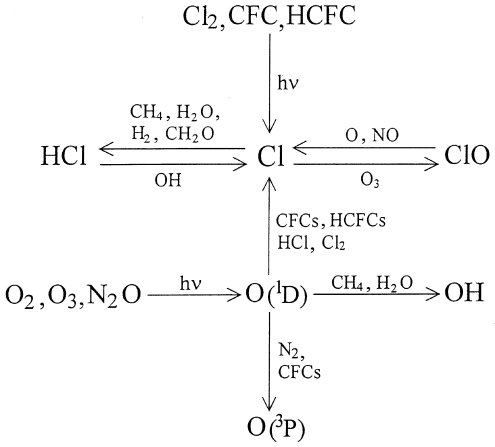

Fig. 1. Chemical cycles for Cl and $O(^1D)$ trace species from Ref. [1]. CFCs, chlorofluorocarbons; HCFCs, hydrochlorofluorocarbons.

followed by chemical reactions of the photochemically produced atoms

$$Cl + O_3 \longrightarrow ClO + O_2,$$

$$Cl + RH \longrightarrow HCl + R\cdot,$$
$$\xrightarrow{} H + R\cdot,$$

$$O(^1D) + N_2 \longrightarrow O(^3P) + N_2(v,J),$$

$$O(^1D) + RCl \longrightarrow ClO + R\cdot,$$
$$\xrightarrow{} Cl + RO\cdot.$$

In this paper, the photodissociation and reaction dynamics of these elementary reactions are studied. It is found that hot

* Corresponding author. Tel.: +81 75 753 5546; fax: +81 75 753 5526; e-mail: masahiro.kawasaki@ae.hines.hokudai.ac.jp

PII S1010-6030(97)00046-4

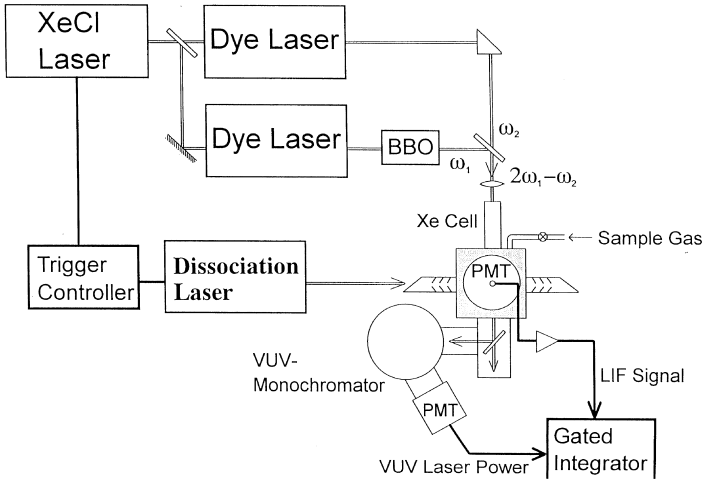

Fig. 2. Schematic diagram of the experimental apparatus for LIF detection in the VUV region.

atoms and radicals are photochemically produced, which are not equilibrated with the surroundings, and react with other molecules before complete thermalization.

2. Experimental details

Fig. 2 shows a schematic diagram of the experimental system used. Photochemically produced atoms were used as reactant species. $O(^1D)$ atoms were generated by the photodissociation of O_3 at 248 nm or N_2O at 193 nm. Cl atoms were produced from Cl_2 or CFCs. For example, in the case of the $Cl + O_3$ reaction, Cl atoms were generated by the photodissociation of Cl_2 at 355 nm. When a mixture of O_3 and Cl_2 was irradiated with the third harmonic (355 nm) of a *Q*-switched YAG laser, ClO was a reaction product. Reaction products of H, D, O and Cl atoms and ClO radicals were probed using vacuum-UV-laser-induced fluorescence (VUV LIF) at 115–180 nm [2]. The probe VUV laser light was generated by four-wave mixing ($2\omega_1 \pm \omega_2$) in Kr or Xe gas or Hg vapour, using two dye lasers both pumped by a single XeCl excimer laser [3]. For the detection of $O(^1D)$ at 115 nm, a tripling technique in a mixture of Kr–Ar gases was used [4].

3. Results and discussion

3.1. Photodissociation of hot ozone [5]

The UV absorption spectrum of ozone consists of two bands: a strong absorption band in the wavelength region 200–310 nm, which is called the Hartley band ($^1B_2 \leftarrow X^1A_1$), and the much weaker band system called the Huggins band in the range 310–360 nm [6]. The Huggins band shows a series of diffuse vibrational structures [7,8]. Spin-allowed dissociation channels in the UV region are

$$O_3 + \hbar\omega \longrightarrow \begin{cases} O(^1D) + O_2(a^1\Delta_g), & \lambda_{th} = 310\ \text{nm} \quad (1) \\ O(^3P) + O_2(X^3\Sigma^-_g), & 1180\ \text{nm} \quad (2) \end{cases}$$

where λ_{th} stands for the thermodynamic threshold of the dissociation wavelength.

We have measured the VUV LIF signal intensities of $O(^1D)$ and $O(^3P)$ as a function of the dissociation wavelength. The quantum yield of $O(^1D)$ from O_3 photolysis at temperatures of 298 and 227 K was calculated from the photofragment yield spectrum using the following expression

$$\Phi_{1D}(\lambda) = \sigma_{1D}(\lambda) / [\sigma_{1D}(\lambda) + \sigma_{3P}(\lambda)] \quad (3)$$

where σ_i is the cross-section of the *i*th species. Fig. 3 shows the wavelength dependence of the quantum yield of $O(^1D)$, together with the yield recommended by JPL/NASA for use in stratospheric modelling [9]. Our data are in agreement

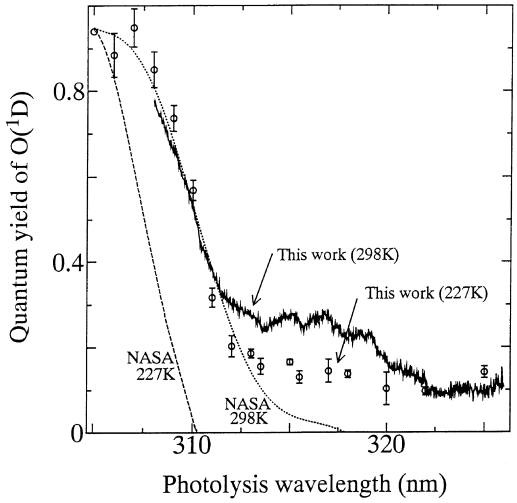

Fig. 3. Wavelength dependence of the quantum yield of $O(^1D)$ atoms produced from O_3 photolysis at 298 K (full curve) and 227 K (filled circles). The dotted curve is the quantum yield of $O(^1D)$ recommended by JPL/NASA for use in stratospheric modelling [9].

with those of recent investigations by Trolier and Wiesenfeld [10] and Ball et al. [11], but not with those of JPL/NASA.

The quantum yield of $O(^1D)$ was almost constant for wavelengths $\lambda \leq 305$ nm and fell sharply around the thermodynamic threshold wavelength of 310 nm for the singlet channel (1). There is considerable controversy concerning the quantum yield of $O(^1D)$ at long wavelengths around 315 nm. JPL recommended values [9] are less than 0.1 at a photolysis wavelength $\lambda < 315$ nm, whereas our measurements, as well as others [10,11], have shown a ''tail'' around 315 nm and yield values of 0.15–0.20 at 315 nm. The ''tail'' in the wavelength range 310–321 nm comes largely from a contribution of hot-band excitation to the repulsive limb of the excited state (2^1A_1).

Global amounts of OH, the primary oxidant of numerous carbon, hydrogen, nitrogen and sulphur compounds, are controlled by the reaction of $O(^1D)$ with H_2O. According to Michelsen et al. [12], the calculated concentrations of $O(^1D)$ and OH for the lower stratosphere are larger by as much as 40% and 15% respectively compared with the results obtained from models which neglect the photolysis of hot O_3. Effects are larger in the lower than in the upper stratosphere because, at lower altitudes, the production of $O(^1D)$ from the photolysis of hot O_3 occurs at longer wavelengths.

3.2. Velocity relaxation of hot $O(^1D)$ atoms [13]

The speed and angular relaxation processes, induced by collisions with He, Ar, Ne, Xe, N_2 and O_2, for the velocity of superthermal $O(^1D)$ photofragments have been studied by measuring the Doppler profiles of $O(^1D)$ as a function of the time delay between the photolysis and probe laser pulses. The nascent $O(^1D)$ atoms, generated in the photodissociation of O_2 by linearly polarized light at 157 nm, have a narrow kinetic energy distribution, centred at 9.8 kcal mol^{-1}, and a large angular anisotropy ($\beta \approx 2$).

$$O_2 + \hbar\omega(157\ \text{nm}) \rightarrow O(^1D) + O(^3P)$$

Fig. 4 shows typical Doppler profiles of $O(^1D)$ atoms at various delay times ($t = 0$–1000 ns) with N_2 as bath gas. A set of Doppler profiles at each delay time was recorded for two different configurations: $k_p \| E_d$ and $k_p \perp E_d$. k_p is the propagation direction of the probe laser and E_d is the direction of the electronic vector of the dissociation laser. The time evolution of the speed distribution under collision conditions is extracted from the Doppler profiles for each bath gas.

$$O(^1D; E_T, \beta) + M \rightarrow O(^1D; E'_T, \beta') + M \quad (4)$$

The anisotropy parameter distribution as a function of the speed at each time delay is also obtained by analysing the Doppler profiles. The distributions thus obtained indicate the following: (1) a collision with He atoms reduces the speed of the $O(^1D)$ atom efficiently, but only changes slightly the direction of its velocity; (2) a collision with N_2 or O_2 reduces the speed of the $O(^1D)$ atom efficiently and almost randomizes the direction of its velocity. Thus the relaxation process

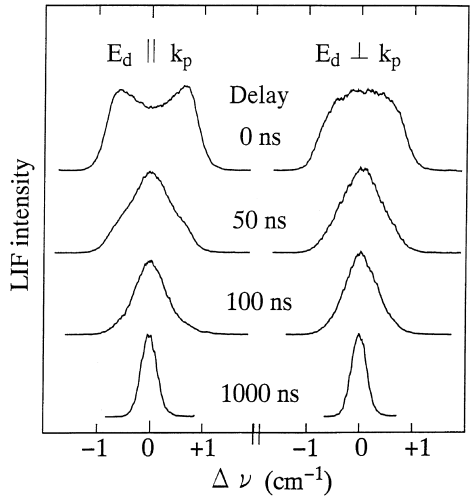

Fig. 4. Velocity relaxation by N_2 (1 Torr) of $O(^1D)$ generated by the 157 nm photodissociation of O_2. Doppler profiles of $O(^1D)$ are shown at various delay times between the photodissociation and probe laser pulses. For comparison, the peak heights of the profiles are normalized with that at $t = 0$. The pressures of O_2 and N_2 are 0.06 and 2.0 Torr respectively. E_d is the direction of the electronic vector of the dissociation laser and k_p is the propagation direction of the probe laser.

depends strongly on the mass ratio of the O atom to the bath gas.

The temporal changes of speed and spatial distribution are expressed as a function of the time delay in a semilogarithmic scale form

$$\langle E(t) \rangle = \langle E(0) \rangle \exp(-k_E t) \quad (5)$$

$$\langle \beta(t) \rangle = \langle \beta(0) \rangle \exp(-k_\beta t) \quad (6)$$

These non-equilibrium relaxation rate constants are summarized in Table 1. Using the collision cross-section for N_2, it is estimated that the rate of translational energy relaxation is comparable with that of the following quenching process

$$O(^1D) + M \rightarrow O(^3P_j) + M \quad (7)$$

In the upper atmosphere, $O(^1D)$ atoms are produced by the photodissociation of O_2 and O_3. For example, O_3 molecules which absorb 250 nm sunlight produce $O(^1D)$ atoms with an average translational energy of 10 kcal mol^{-1}. On the basis of our measurements of the quenching and energy dissipation rates, about half of the $O(^1D)$ atoms are quenched with 1 Torr of N_2 before thermalization of the translational energy is accomplished. It has been widely accepted that the translationally hot $O(^1D)$ atoms are quickly relaxed by collisions with atmospheric air and entirely thermalized before they react with other molecules, such as HCl, H_2O and N_2O. However, our results indicate that the translational energy of the hot $O(^1D)$ atoms produced photochemically is not fully equilibrated with the surroundings, and reactions may take place before complete thermalization.

The electronic energy transfer efficiencies to the internal energy of N_2, CO, CO_2 and CF_3H are also obtained from the Doppler profile measurement of $O(^3P_j)$ atoms in the quenching reaction. The efficiencies are $30\% \pm 7\%$, $31\% \pm 7\%$,

Table 1
Translational energy and anisotropy relaxation rate constants and collisional radii for $O(^1D)$ with rare gas atoms, N_2 and O_2. k_E and k_β denote the collisional relaxation rate constants for energy and angular anisotropy relaxation respectively, which are defined in Eq. (5) and Eq. (6). d_E and d_β denote the hard-sphere collisional radii for energy and angular anisotropy relaxation respectively

Collision partner	Mass ratio [a]	k_E (10^{-10} cm^3 molecule^{-1} s^{-1})	k_β (10^{-10} cm^3 molecule^{-1} s^{-1})	d_E (Å)	d_β (Å)
He	0.25	1.00	0.7	2.2	2.6
Ne	1.25	1.4	2.1	2.1	1.9
Ar	2.50	1.3	4.1	2.2	2.5
N_2	1.75	2.0	3.2	2.8	2.2
O_2	2.00	1.5	2.5	2.4	1.9

[a] Ratio of mass of collision partner to mass of oxygen atom.

49% ± 3% and 52% ± 5% respectively. The large efficiencies imply that these systems form a complex as an intermediate

$$O(^1D) + M \rightarrow [O-M]^{\ddagger} \rightarrow O(^3P) + M(v,J) \quad (8)$$

For example, the rotational distribution of a CO molecule excited by collision with a translationally hot $O(^1D)$ atom was measured by probing the product CO [14]. The inelastic collisions are of two types. Adiabatic collisions involve motion on the first excited singlet surface of the CO_2 system

$$\text{Hot } O(^1D) + CO \rightarrow O(^1D) + CO(v \leq 1,J) \quad (9)$$

whereas non-adiabatic collisions begin on this singlet surface but end on the lowest triplet surface before dissociation to $O(^3P)$ and CO

$$O(^1D) + CO \rightarrow O(^3P) + CO(v \leq 9,J) \quad (10)$$

The measured rotational distributions are interpreted using these two different pathways. Fig. 5 shows the rotational distributions of the product CO in $v = 0$, 1, 2 and 3. The measured rotational distributions for CO ($v = 2$ and 3), which can only come from non-adiabatic collisions, agree with the results of a trajectory calculation performed on the ab initio lowest triplet potential energy surface of CO_2. However, the rotational distributions measured for CO ($v = 0$ and 1) show a significant difference from the trajectory calculation. This is because excitation of the $v = 0$ and 1 levels can be accomplished by either adiabatic (singlet surface) or non-adiabatic (triplet surface) collisions. The vibrational distributions of CO excited by collision with thermal $O(^1D)$ atoms were also measured to be $v = 1/2/3/4/5/6 = 1/0.52/0.29/0.25/0.17/0.11$. These results are in good agreement with our trajectory calculation at the MP2/6-31G* level. Similar energy transfer processes are expected for $O(^1D) + N_2$ via the singlet and triplet surfaces of N_2O.

3.3. Reaction of $O(^1D)$ atoms with alkanes and alkyl chlorides [15]

H and D product atoms from the reaction of $O(^1D)$ with alkanes and alkyl chlorides were measured

$$O(^1D) + RH \rightarrow H + RO \quad (11)$$

The observed isotopic branching ratios [H]/[D] in the reactions of $O(^1D)$ with $CH_3CD_2CH_3$, $CD_3CH_2CD_3$, $CD_3CHClCD_3$ and $CH_3CDClCH_3$ are almost statistical at collision energies of 8.1–9.1 kcal mol^{-1}. Fig. 6 shows the Doppler profile of the H atoms from the reactions of $O(^1D) + CH_4$. The Doppler profiles of the H atoms from the reactions of $O(^1D)$ + alkanes (CH_4, C_2H_6 and C_3H_8) suggest that the translational energy released to the RO + H products (mainly in the H atom) is 8 ± 1 kcal mol^{-1} and is almost independent of the size of the alkyl group.

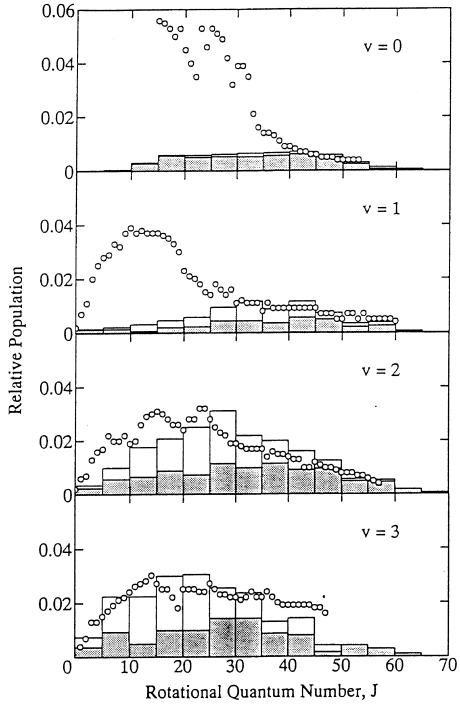

Fig. 5. Rotational populations for $v = 0$, 1, 2 and 3 of collisionally produced CO with hot $O(^1D)$. Circles give the experimental results. Bars give the results of the trajectory calculations for the non-adiabatic collisions. Shaded bars are non-atom exchange reactions ($O + CO^* \rightarrow O + CO(v,J)$) and white bars are oxygen atom exchange reactions ($O + CO^* \rightarrow CO(v,J) + O^*$).

The statistical [D]/[H] ratios imply that $O(^1D)$ atoms insert indiscriminately into the primary and secondary C–H bonds of RH. An important characteristic of the O–H bond is the fact that the mass of the H atom is very small compared with that of the organic fragment. Such an O–H detachment process may have little effect on the atoms not bonded to the same O atom. In other words, only atoms bonded to the O atom actively participate in sharing energy with the departing

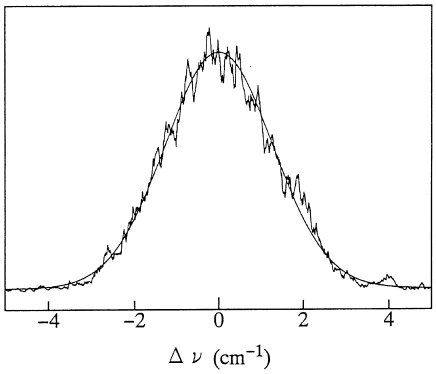

Fig. 6. Doppler profile of H atoms from the reaction of $O(^1D)$ with CH_4. The mixture of O_3 (8 mTorr) and CH_4 (60 mTorr) was irradiated with a 248 nm KrF laser, and the H atoms produced were detected by LIF at 121.6 nm. The full line is a simulated curve for a gaussian profile of 8 kcal mol^{-1} width in the Maxwell velocity distribution.

H atom. A similar discussion has been given for the C–H cleavage in the photodissociation of chloroethylenes [16].

The relative quantum yields estimated for the H atom formation process over the total reaction process are summarized in Table 2 and Table 3. Except for CH_4, the major process for RH is not OH formation but C–C bond cleavage, because energy flow in the hot alcohol intermediates is smooth for the C–C and C–O bonds. However, since the kinetic energy distributions of the H atoms produced in the reactions are almost the same for CH_4, C_2H_6 and C_3H_8, the energy participation for H atom formation is localized near the O–H bond. With increasing number of H atoms in the molecule, the relative quantum yields of H and Cl production increase for $O(^1D) + RCl$. These ratios are, however, much smaller than the number ratios of H and Cl atoms in the reactant molecule. On an energetic basis, the Cl formation process is much more exoergic than the H formation process, and hence insertion/decomposition at the C–Cl bond is more favourable than that at the C–H bond. The release of Cl atoms is also favoured over H atoms because the electronic degeneracy of a $Cl(^2P_{3/2})$ atom is greater than that of an $H(^2S)$ atom.

Table 2
Product branching ratios in the reactive collision between $O(^1D)$ and RH at thermal collision energies

RH	Φ_H [a]	Φ_{OH} [b]	Φ_{Cl} [c]	Φ_q [d]	Φ_{other} [e]
CH_4	0.14	0.86	–	0	0
C_2H_6	0.10	0.03	–	0	0.87
C_3H_8	0.08	0.06	–	0	0.86
CH_3Cl	0.07	n.d.	0.26	0.09	$0.58 - \Phi_{OH}$

[a] Obtained from [H]/[D] ratio from a 1 : 1 mixture with D_2.
[b] OH formation.
[c] Obtained from [H]/[Cl] ratio.
[d] Physical quenching process, $O(^1D) + RH \rightarrow O(^3P) + RH$.
[e] Yield of residual process including C–C bond cleavage, HCl formation, etc.

Table 3
Relative quantum yields of H and $Cl(^2P_{3/2})$ product atoms in the reaction of $O(^1D)$ with RCl

Reactant	Φ_H/Φ_{Cl} [a]
CH_3Cl	0.27
C_2H_5Cl	1.1 ± 0.2
2-C_3H_7Cl	0.91 ± 0.17

[a] The $Cl(^2P_{1/2})$ yield is less than 10% of the $Cl(^2P_{3/2})$ yield. The error is one standard deviation for 5–10 experimental runs.

3.4. Formation of vibrationally excited ClO radicals [17]

ClO radicals are detected by the LIF method with the $C^2\Sigma - X^2\Pi$ $(0,v'')$ system at 167–180 nm. Fig. 7 shows an excitation spectrum of the thermalized ClO $C^2\Sigma - X^2\Pi_{3/2}$ (0,0) band. The intensity distribution of the experimentally obtained spectrum is well reproduced by the simulated spectrum as shown in Fig. 7.

The nascent vibrational distribution of the $ClO(X^2\Pi)$ radicals produced in the ozone destruction reaction has been measured

$$Cl + O_3 \rightarrow ClO(\leq 17) + O_2 \quad (12)$$

The nascent vibrational distribution of the ClO radicals is shown to be strongly inverted, with the relative ratio $v = 0/1/2/3/4/5 = 0.8/1/1.3/2.4/2.9/2.7$. Fig. 8 shows the surprisal plots [18] for the nascent ClO. The prior distributions of the vibrational states in the ClO products were calculated using the rigid rotor harmonic oscillator approximation. The slope of the linear surprisal plots, λ_v, for the ClO radicals from reaction (12) is strongly negative with a coefficient of -8, suggesting that ClO is highly vibrationally excited.

The vibrational relaxation processes for the ClO radicals in the $X^2\Pi$ state by collisions were also studied in our experiment. The upper limit value of the vibrational relaxation rate constant for ClO $(v = 1 \rightarrow 0)$ by collisions with N_2 is esti-

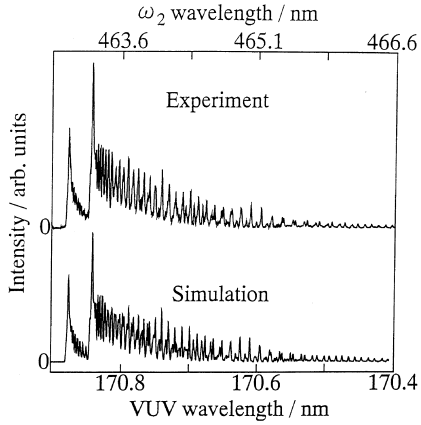

Fig. 7. Fluorescence excitation spectra of the ClO $C^2\Sigma - X^2\Pi_{3/2}$ (0,0) band. Upper trace: experimentally obtained spectrum of ClO from the reaction between $O(^1D)$ and CCl_3F. The pressures were: O_3, 10 mTorr; CCl_3F, 100 mTorr; Ar, 1 Torr. The delay time between the photolysis and probe laser was 40 μs. Lower trace: simulated spectrum with a rotational temperature of 300 K.

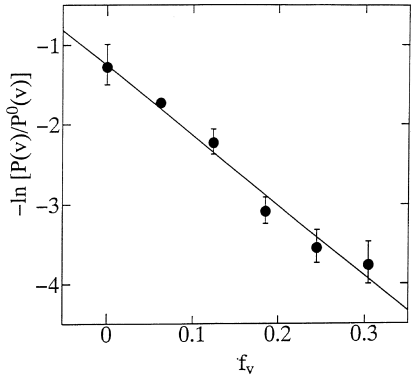

Fig. 8. Surprisal plots for the vibrational population of ClO radicals produced from the reaction of $Cl + O_3$. f_v is the fraction of the total available energy in the product vibration. The slope of the full line for the linear surprisal is −8.

mated to be 5×10^{-14} cm^3 molecule^{-1} s^{-1}. Recently, Gericke [19] found $k\approx1\times10^{-14}$ cm^3 molecule^{-1} s^{-1} using two-photon absorption of ClO ($C^2\Sigma$, $v'=1,0$ to $X^2\Pi_{3/2}$, $v''=0$–7).

The pressure of atmospheric N_2 is about 2 Torr at 40 km altitude. Gericke's [19] value for the vibrational relaxation with N_2 corresponds to a reaction rate of 6×10^2 s^{-1} under these conditions. This value of the relaxation rate is much faster than the reported reaction rate of the ground state of ClO ($v=0$) in the stratosphere. However, if the rates of reactions involving vibrationally excited ClO are much faster than those for ClO ($v=0$), the reactions of vibrationally excited ClO radicals may be important in the atmosphere.

According to Matsumi and Shamsuddin [20], when ClO radicals are produced by reactions with CFCs, e.g.

$$O(^1D) + CCl_3F \rightarrow ClO(X^2\Pi) + CCl_2F \quad (13)$$

the nascent ClO radical is highly vibrationally excited due to the large exothermicity of the reaction. Recently, Delmdahl et al. [21] reported high vibrational excitation of ClO from the ClO_2 photodissociation at 308 and 351 nm using a two-photon-induced fluorescence technique. Vanderzanden and Birks [22] observed oxygen atoms in the reaction system $Cl + O_3$. The appreciable role of vibrationally excited ClO radicals in the $Cl + O_3$ reaction system has been pointed out. Choo and Leu [23] suggested two possible schemes for O atom production: vibrationally excited ClO (v) radicals produced by the reaction of $Cl + O_3$ react with O_3 molecules or Cl atoms

$$ClO(v) + O_3 \rightarrow ClO + O_2 + O \quad (14)$$

The activation energies for the reactions of ClO with O_3, CH_4, H_2, CO and N_2O are equal to or larger than about 8 kcal mol^{-1} [9]. Thus vibrationally hot ClO may have an impact on our understanding of atmospheric reactions.

3.5. Product branching ratios for O(^{3}P) atom and ClO radical formation in the reactions of O(^{1}D) with chloro compounds [24]

Chloro compounds, such as CFCs and chloromethanes, are of global concern due to their potential for the drastic reduction of stratospheric ozone concentrations [25,26]. When these molecules eventually diffuse into the stratosphere, they undergo reactions with $O(^1D)$ as well as UV photolysis. The chemical reactions of $O(^1D)$ play a major role in establishing the chemical composition of the stratosphere [27]. Therefore collisional quenching and the reactions of $O(^1D)$ with collision partners with varying degrees of chlorination are of great interest.

Quenching of $O(^1D)$ atoms with CFCs and other molecules produces $O(^3P_j)$ atoms

$$N_2O + 193\ \text{nm} \rightarrow O(^1D) + N_2$$

$$O(^1D) + M \rightarrow O(^3P_2) + M\ \Delta H = -45\ \text{kcal mol}^{-1}$$

where M is a collision partner. The temporal profiles of the VUV LIF signal of $O(^3P_2)$ were measured for delay times up to 25 μs. Typical examples are shown in Fig. 9 for $O(^1D) + N_2$ and $O(^1D) + CH_3F$. N_2 quenches $O(^1D)$ to $O(^3P)$ with unit efficiency and with the following rate constant [9]

$$O(^1D) + N_2 \rightarrow O(^3P) + N_2$$

$$k = 2.6\times10^{-11}\ \text{cm}^3\ \text{molecule}^{-1}\ \text{s}^{-1}$$

The asymptotic VUV LIF signal intensity for each of the various collision partners is compared with that of N_2 to obtain the branching ratios Φ_q for the quenching of $O(^1D)$ to $O(^3P_j)$. When the collision partners of $O(^1D)$ are chlorinated compounds, ClO radicals are generated. We also measured the temporal profile of ClO production with the VUV laser wavelength fixed at the Q_1 branch bandhead of the (0,0) band. The results are summarized in Table 4, together with those of previous investigations. Sums of the branching ratios for the $O(^3P)$ atom and ClO radical formation are almost unity for $O(^1D)$ + chlorofluoromethanes. The branching ratios are less than unity for $O(^1D)$ + chloromethanes because the OH formation channel is open for the latter.

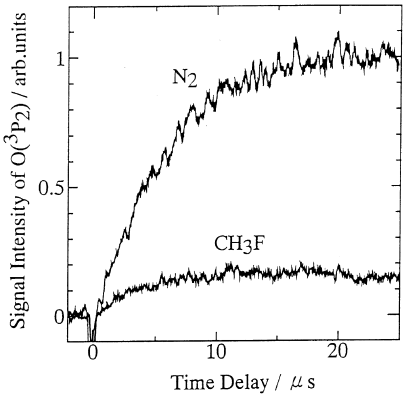

Fig. 9. Temporal profiles of the VUV LIF signal of $O(^3P_2)$ produced from $O(^1D) + N_2$ and $O(^1D) + CH_3F$. $O(^1D)$ was produced from the photodissociation of N_2O at 193 nm. The pressures of N_2O, CH_3F and Ar were 1 mTorr, 50 mTorr and 2 Torr respectively. The probe laser wavelength was fixed at the centre of the resonance line for $O(3s^3S^0 \leftarrow 2p^3P_2)$. The horizontal scale is the time delay between the photolysis and probe laser pulses.

Table 4
Rate constants for the reaction of $O(^1D)$ with chlorofluorocarbons, chloromethanes and hydrofluorocarbons at room temperature

Collision partner	k (10^{-10} cm^3 molecule^{-1} s^{-1})		
	k_q [a]	k_{ClO} [b]	k_{total} [c]
CCl_4	0.5 [d]	3.0	3.3
$CFCl_3$	0.3 [d]	2.0	2.3
CF_2Cl_2	0.3	1.2	1.4
CF_3Cl	0.2	0.7	0.87
$CHCl_3$	0.4 [d]	2.1	3.0
CH_2Cl_2	0.2 [d]	1.7	2.7
CH_3Cl	0.2 [d]	1.0	2.1
CH_3F	0.3		1.5
CH_2F_2	0.4 [e]		0.51
CHF_3	0.07		0.091
CF_4	0.0002 [f]		0.0002

[a] Quenching to $O(^3P_j)$.
[b] ClO formation.
[c] Total rate constant for removal of $O(^1D)$. Values for $O(^1D)$ + chloromethanes are taken from Ref. [28], and others from Ref. [9].
[d] Ref. [28].
[e] Ref. [29].
[f] Ref. [9].

Acknowledgements

The author thanks Dr Yutaka Matsumi for his cooperation, the Heiwa Nakajima Foundation, and the Japan Society for Promotion of Science for partial financial support.

References

[1] R.R. Wayne, Chemistry of Atmosphere, Clarendon Press, 1994.
[2] Y. Matsumi, S.M. Shamsuddin, M. Kawasaki, J. Chem. Phys. 101 (1994) 8262.
[3] G. Hilber, A. Lago, R. Wallenstein, J. Opt. Soc. Am. B 4 (1987) 1753.
[4] R. Hilbig, R. Wallenstein, IEEE J. Quantum Electron. 17 (1981) 1566.
[5] K. Takahashi, Y. Matsumi, M. Kawasaki, J. Phys. Chem. 100 (1996) 4084.
[6] J.I. Steinfeld, S.M. Adler-Golden, J.W. Gallagher, J. Phys. Chem. Ref. Data 16 (1987) 911.
[7] J.W. Simons, R.J. Paur, H.A. Webster III, E.J. Bair, J. Chem. Phys. 59 (1973) 1203.
[8] J.A. Joens, J. Chem. Phys. 101 (1994) 5431.
[9] W.B. DeMore, S.P. Sander, C.J. Howard, A.R. Ravishankara, D.M. Golden, C.E. Kolb, R.F. Hampson, M.J. Kurylo, M.J. Molina, Chemical Kinetics and Photochemical Data for Use in Stratospheric Modeling, Evaluation No. 11, JPL Publication 94-26, Pasadena, CA, 1994.
[10] M. Trolier, J.R. Wiesenfeld, J. Geophys. Res. 93 (1988) 7119.
[11] S.M. Ball, G. Hancock, I.J. Murphy, S.P. Rayner, Geophys. Res. Lett. 20 (1993) 2063.
[12] H.A. Michelsen, R.J. Salawitch, P.O. Wennberg, J.G. Anderson, Geophys. Res. Lett. 21 (1994) 2227.
[13] Y. Matsumi, S.M. Shamsuddin, Y. Sato, M. Kawasaki, J. Chem. Phys. 101 (1994) 9610. Y. Matsumi, S.M.S. Chawdhury, J. Chem. Phys. 104 (1996) 7036.
[14] M. Abe, Y. Inagaki, L.L. Springsteen, Y. Matsumi, M. Kawasaki, H. Tachikawa, J. Phys. Chem. 98 (1994) 12 641.
[15] Y. Matsumi, K. Tonokura, Y. Inagaki, M. Kawasaki, J. Phys. Chem. 97 (1993) 6816.
[16] Y. Mo, K. Tonokura, Y. Matsumi, M. Kawasaki, T. Sato, T. Arikawa, P.T.A. Reilly, Y. Xie, Y. Yang, Y. Huang, R. Gordon, J. Chem. Phys. 97 (1992) 4815.
[17] Y. Matsumi, S. Nomura, M. Kawasaki, T. Imamura, J. Phys. Chem. 100 (1996) 176.
[18] R.D. Levine, R.B. Bernstein, Acc. Chem. Res. 7 (1974) 393.
[19] S. Baumgänter and K.-H. Gericke, Chem. Phys. Lett. 227 (1994) 461.
[20] Y. Matsumi, S.M. Shamsuddin, J. Chem. Phys. 103 (1995) 4490.
[21] R.F. Delmdahl, S. Baumgaertel, K.-H. Gericke, J. Chem. Phys. 104 (1996) 2883.
[22] J.W. Vanderzanden, J.W. Birks, Chem. Phys. Lett. 88 (1982) 109.
[23] K.Y. Choo, M.T. Leu, J. Phys. Chem. 89 (1985) 4832.
[24] K. Takahashi, R. Wada, Y. Matsumi, M. Kawasaki, J. Phys. Chem. 100 (1996) 10145.
[25] M.J. Molina, F.S. Rowland, Nature 249 (1974) 810.
[26] F.S. Rowland, M.J. Molina, Rev. Geophys. Space Phys. 13 (1975) 1.
[27] R.J. Cvetanovic, Can. J. Chem. 52 (1974) 1452.
[28] J.A. Coxon, W.E. Jones, E.G. Skolnik, Can. J. Phys. 54 (1976) 1043.
[29] A.R. Ravishankara, S. Solomon, A.A. Turnipseed, R.F. Warren, Science 259 (1993) 194.